

Enhanced Catalytic Reduction of *p*-Nitrophenol Using Anodic Aluminum Oxide-Supported Gold Nanoparticles: A Comparative Study of Membrane and Wire Forms

Nurul Hanis Nabilah Ahmad Faizal¹, Hanani Yazid^{2*} and Abdul Mutalib Md Jani³

^{1,2}Faculty Applied Sciences, Universiti Teknologi MARA, Perlis Branch, Arau Campus, 02600 Arau, Perlis, Malaysia

³Faculty of Applied Sciences, Universiti Teknologi MARA, Perak Branch, Tapah Campus, 35400 Tapah Road, Perak, Malaysia

*Corresponding author (e-mail: hanani946@uitm.edu.my)

Anodic aluminum oxide (AAO) has emerged as a robust catalyst support due to its superior mechanical properties and thermal stability. Fabricated through a two-step electrochemical anodization process, AAO can be tailored into membrane and wire forms, offering control over pore size, alignment, and thickness by adjusting anodization parameters such as voltage and electrolytes. While AAO membranes have been extensively studied, the potential of AAO wires as catalyst support remains under-explored. This study aims to evaluate the catalytic performance of AAO in both membranes and wires form as supports for gold nanoparticles (Au NPs) in the reduction of *p*-nitrophenol (*p*-NP). AAO membrane (mAAO) and wire (wAAO) were fabricated under similar anodization parameters and immobilized with Au NPs via deposition-precipitation (DP) technique yielding Au/mAAO and Au/wAAO catalysts. Characterization by Fourier Transform Infrared Spectroscopy (FTIR) confirmed successful Au immobilization with notable shifts in the O-H bond (~3400 cm⁻¹) and Si-O bond (~1000 cm⁻¹). Field-Emission Scanning Electron Microscopy (FE-SEM) further demonstrated uniform pore distribution of AAO and well-dispersed Au NPs yielding values of 76.75 ± 11.29 nm and 16.03 ± 5.54 nm for Au/mAAO while for Au/wAAO are 74.97 ± 10.49 nm and 18.43 ± 11.16 nm, respectively. Additionally, the XRD instrument was utilized to investigate the amorphous patterns and nanocrystalline properties of the modified AAO forms. The % Au loadings show the value of 0.88 wt% (Au/mAAO) and 0.92 wt% (Au/wAAO). Catalytic activity was assessed via Ultraviolet-Visible Spectroscopy (UV-Vis) revealed that Au/mAAO exhibited significantly higher rate constants ($k = 4.24 \times 10^{-3} \text{ s}^{-1}$) compared to Au/wAAO ($k = 4.31 \times 10^{-4} \text{ s}^{-1}$) highlighting the superior performance of the membrane form.

Keywords: Anodic aluminum oxide (AAO); gold nanoparticles (Au NPs); deposition-precipitation (DP); *p*-nitrophenol; catalytic activity

Received: September 2024; Accepted: December 2024

Aluminum (Al) is a major component of the Earth's crust, comprising approximately 8% of its composition. Its reactivity with atmospheric oxygen leads to the formation of aluminum oxide (Al₂O₃), commonly known as alumina [1]. Alumina can be synthesized through electrochemical anodization, a method that forms anodic aluminum oxide (AAO). This technique involves a two-step anodization process, allowing for precise control over AAO's geometric structures by adjusting parameters such as potential voltage, temperature, and electrolyte concentration [2]. The first step in the two-step anodization process involves the ionization of high-purity aluminum, followed by chemical etching with chromic acid (H₂CrO₄) or phosphoric acid (H₃PO₄). This etching is essential for ensuring morphological consistency of the AAO template by removing uneven aluminum oxide patterns, resulting in a well-ordered surface for subsequent anodization [3, 4]. The second anodization phase focuses on pore nucleation at surface flaws,

establishing precise pore growth sites. Consistent conditions from the first step are maintained to control the final AAO thickness, particularly for membranes [3].

The anodization process of aluminum foil and wire produces anodic aluminum oxide (AAO) in the form of a membrane and wire, respectively. The AAO is an inert support; however, modification of its surface is necessary to improve its reactivity. Commonly, after the fabrication of the AAO, its surface is modified by a hydroxy-silanization process. This process adds the amino group to the AAO surface, extending the applications of the AAO [5]. Additionally, both forms of AAO exhibit strong mechanical properties, excellent thermal stability, and a large surface area, making AAO a promising support for various metal nanoparticles, such as gold (Au) [6]. Supported Au NPs can be effectively synthesized by deposition-precipitation (DP). The DP method

was chosen in this study due to its effectiveness in producing highly dispersed and uniformly deposited Au NPs on oxide supports. This method allows for precise pH adjustment during catalyst synthesis, a critical factor in achieving optimal nanoparticle characteristics and catalytic performance [7]. The pH adjustment promotes the transformation of the Au precursor into active species that precipitate as hydroxides on the AAO surface, with the AAO acting as a nucleation site to anchor these species, resulting in robust, well-integrated catalytic support [8].

Au NPs deposited on AAO surfaces were evaluated for their catalytic effectiveness in reducing *p*-nitrophenol (*p*-NP), a toxic pollutant prevalent in wastewater from pesticides, chemical petroleum, dye, and other industrial sectors [9]. The reduction of *p*-NP is converted into a less toxic and more industrially valuable intermediate, *p*-aminophenol (*p*-AP) during catalytic reduction. Thus, the study aims to compare the activity of AAO in membranes and wire forms as support for Au NPs for the application in the reduction of *p*-NP. Both the AAO membrane and wire forms were fabricated using similar anodization parameters (electrolyte, voltage, and temperature), followed by the deposition-precipitation (DP) technique to deposit Au onto the AAO surface, resulting in the Au/mAAO and Au/wAAO catalysts. The catalytic performance was studied kinetically based on the pseudo-first order and the rate constant value was calculated to determine their activity. The kinetic reaction is monitored using UV-Visible (UV-Vis) spectrophotometry.

EXPERIMENTAL

Chemicals and Materials

A high-purity tetrachloroauric acid ($\text{HAuCl}_4 \cdot 3\text{H}_2\text{O}$), sodium hydroxide (NaOH), and 3-aminopropyl-triethoxysilane (APTES, $\text{C}_9\text{H}_{23}\text{NO}_3\text{Si}$, 98%) were supplied by Sigma-Aldrich (USA). Both aluminum forms, aluminum foil with a thickness of 0.1 mm (metal basis 99.997%) and aluminum wire with a thickness of 1.0 mm (metal basis 99.9995%) were purchased by Thermo Fischer Scientific (Massachusetts, USA). *p*-Nitrophenol (*p*-NP), phosphoric acid (H_3PO_4 , 85%), and hydrogen peroxide (H_2O_2 , analytical reagent grade 30%) were acquired from Merck (Darmstadt, Germany). Oxalic acid ($\text{C}_2\text{H}_2\text{O}_4$), hydrochloric acid (HCl), and toluene ($\text{C}_6\text{H}_5\text{CH}_3$) were purchased from R&M Chemicals Ltd. Sodium borohydride (NaBH_4) was purchased from Friendemann Schmidt. Lastly, acetone ($\text{C}_3\text{H}_6\text{O}$, 99%), ethanol ($\text{C}_2\text{H}_6\text{O}$, 95%), and copper(II) chloride dihydrate ($\text{CuCl}_2 \cdot 2\text{H}_2\text{O}$, 99%) were obtained from a commercial supplier, HmbG.

Fabrication of AAO Membrane and Wire

A high-purity aluminum (Al) foil (metal basis 99.997%, 0.1 mm, Alfa Aesar) measuring 2 cm \times 2 cm and aluminum wire (99.995%, 1.0mm, Alfa Aesar) with a

length of 10 cm were fabricated using a two-step anodization procedure. Before anodization, the aluminum foil was pre-treated by sonication in acetone ($\text{C}_3\text{H}_6\text{O}$ (99%), HmbG), ethanol ($\text{C}_2\text{H}_6\text{O}$ (95%), HmbG), and distilled water for five minutes each [5]. Similarly, the aluminum wire was sonicated in acetone and distilled water for five minutes followed by a two-step electrochemical anodization process [10]. The anodization was conducted within an electrochemical cell, where the aluminum (Al) served as the anode and lead (Pb) as the cathode. This process was performed at 80 V for one minute at a controlled temperature of 5 °C using an electrolyte solution of 250 mL of 0.30 M oxalic acid ($\text{C}_2\text{H}_2\text{O}_4$, Bendosen) with vigorous stirring. Subsequently, the initial layer of the AAO membrane was removed by immersion in a phosphochromic acid solution ($\text{H}_3\text{PO}_4 \cdot \text{CrO}_3$) at 60 °C for one hour, followed by a second anodization step at 60 V for four hours under the same electrolyte and temperature condition of 5 °C [5]. For the aluminum wire, the etching step was performed at 80 °C for two hours [10]. After the anodization, the unreacted aluminum foil was selectively removed from the membranes by immersion in a solution containing 5 wt% of copper (II) chloride dihydrate ($\text{CuCl}_2 \cdot 2\text{H}_2\text{O}$ (99%), HmbG) and 15 wt% of hydrochloric acid (HCl, MERCK). The AAO structures were then left to dry at room temperature, after which three drops of 1.15 M phosphoric acid solution (H_3PO_4 (85%), MERCK) were applied to the backside of membranes to open the bottom pores [5].

Surface Functionalization by APTES

Subsequently, the AAO membrane and wire were subjected to hydroxylation by immersion in the hydrogen peroxide solution (H_2O_2 , analytical reagent grade 30%, MERCK). The AAO samples were immersed in the solution at 80 °C for 30 minutes. Following hydroxylation, the AAO was left to dry at room temperature. The hydroxylated AAO (AAO-OH) was then subjected to silanization. This was achieved by immersing the AAO in a 5 mL solution containing 250 μL of 3-aminopropyl-triethoxysilane ($\text{C}_9\text{H}_{23}\text{NO}_3\text{Si}$ (98%), Sigma Aldrich) and 4.75 mL of toluene ($\text{C}_6\text{H}_5\text{CH}_3$, HmbG) and immersed for overnight [5].

Preparation of Au/mAAO and Au/wAAO by Deposition-Precipitation (DP) Method

The gold (Au) precursor used was high-purity tetrachloroauric acid ($\text{HAuCl}_4 \cdot 3\text{H}_2\text{O}$ (>99.9%), Sigma Aldrich). A total of 0.0788 g of the gold (Au) precursor was dissolved in 50 mL of distilled water to prepare a gold (Au) solution of 4.0 mM. Subsequently, 10 mL of the prepared Au solution was heated to 80 °C for approximately 10 minutes. The pH of the solution was then carefully adjusted to 8 by the dropwise addition of 0.25 M sodium hydroxide (NaOH, Sigma-Aldrich). The AAO membrane and wire were immersed separately in the prepared Au solution and sonicated for 30 seconds to facilitate

uniform dispersion. The mixture was then subjected to a 4-hour aging process to allow sufficient deposition of gold onto the AAO supports. After aging, the AAO samples were thoroughly rinsed and sonicated with 10 mL of distilled water four times, each for 30 seconds, to remove any unreacted gold precursor. Finally, the AAO membrane and wire were calcined at 400 °C in the air for two hours to complete the deposition process and stabilize the gold nanoparticles [11].

Catalyst Characterization Methods

The Au/mAAO and Au/wAAO catalysts were characterized using FTIR, FE-SEM, XRD, ICP-OES, and UV-Vis. The surface chemical properties of the modified anodic aluminum oxide nanoporous membrane and wire were analyzed using the Fourier Transform Infrared spectrometer, FTIR (Frontier, Perkin Elmer). The FTIR spectra were acquired with a Perkin Elmer Spectrum One spectrometer, equipped with an Attenuated Total Reflectance (ATR) module featuring a diamond crystal at the center of the circular mounting plate. The instrument operated over a scanning range of 400–4000 cm^{-1} . The synthesized Au/mAAO and Au/wAAO morphology were examined by Field-Emission Scanning Electron Microscopy, FE-SEM (Nova Nanosem 450, FEI). A small amount of each sample was placed on carbon tape and coated with a thin layer of platinum. The operational parameters of the FE-SEM were set to 15 kV, with a working distance between 4.5 and 4.7 mm, allowing for magnification up to 100k \times magnification [12]. The magnification could be further increased for more detailed imaging of the AAO samples. The samples were then subjected to an electron beam, and the resulting images were recorded for detailed analysis.

X-ray diffraction, XRD (X'Pert Pro, PAN analytical) analysis was conducted to examine the amorphous patterns and nanocrystalline properties of the synthesized AAO. Characterization was performed with a diffractometer utilized with Cu-K α radiation at 40 kV, scanning for two thetas (θ) angles from 20° to 80°. The Au loading in both prepared catalysts, Au/mAAO and Au/wAAO, was quantified using an Inductively Coupled Plasma-Optical Emission Spectrometer (ICP-OES, Optima 8000, Perkin Elmer). For ICP-OES analysis, the catalysts were digested in aqua regia, diluted with deionized water, and filtered through a 0.45 μm membrane filter prior to the analysis. The Au content (wt%) was calculated using the following formula: $\text{Au (\%wt.)} = (\text{mass of Au}) / (\text{mass of catalyst}) \times 100$ [5]. Lastly, the catalytic activity of the samples was evaluated by Ultraviolet-Visible, UV-Vis spectrophotometer (Lambda 25, Perkin Elmer) focusing on the reduction process of *p*-nitrophenol (*p*-NP) to *p*-aminophenol (*p*-AP). The reduction process was monitored by tracking the absorbance peak intensity at 400 nm, adhering to a pseudo-first-order kinetic model [5]. UV-Vis measurements

were recorded at 1-minute intervals at a wavelength of 400 nm.

Catalytic Study

The catalytic performance of the Au/AAO membrane (Au/mAAO) was evaluated through the reduction of *p*-nitrophenol (*p*-NP). 1 mg of Au/mAAO catalyst was added to a cuvette containing 1.5 mL of freshly prepared 15.0 mM sodium borohydride solution (NaBH_4 , Riendemann Schmidt Chemical). Subsequently, 1.5 mL of 0.05 mM *p*-nitrophenol solution (*p*-NP, MERCK) was introduced into the cuvette, initiating the reaction upon mixing. The catalytic activity was monitored using Ultraviolet-Visible spectrophotometer, UV-Vis (Lambda 25, Perkin Elmer) which tracked the reduction process by observing the decrease in absorbance at 400 nm over time. The UV-Vis measurements were conducted at 1-minute intervals at a wavelength of 400 nm in a quartz cuvette. The rate constant value (k) was determined by plotting $\ln(A/A_0)$ against time [11]. The slope of the linear regression from this plot provided the rate constant for the pseudo-first-order reaction [5]. This methodology was also applied to analyze the catalytic performance of Au/wAAO.

RESULTS AND DISCUSSION

Nanoporous AAO

AAO Membrane (mAAO)

Figure 1 illustrates the electrochemical transformation process of Al to mAAO produced from a high-purity aluminum (Al) foil as presented in **Figure 1(a)** followed by a chemical etching process in a mixed solution of 1.8 wt.% chromic acid and 6 wt.% of phosphoric acid as shown in **Figure 1(b)**. After the first anodization, the etching process was utilized to ensure the production of ordered hexagonal pores by improving the aluminum's surface through the removal of the oxidized layer on the Al surface for subsequent anodization [4]. **Figure 1(c)** shows the mAAO after the second anodization while **Figure 1(d)** depicts the mAAO after detachment of Al foil. The anodization of the Al yielded the AAO due to the reaction between the Al and the oxalate anion ($\text{C}_2\text{O}_4^{2-}$) present in the electrolyte. The surface color of the mAAO was changed from silver to yellow, a change attributable to several factors, including pore modification, optical interference, and diffraction. The anodization process induces modifications in pore size, distribution, and overall structure, affecting the optical properties and resulting in color shifts [13]. The observed color is also influenced by optical interference and diffraction, where light interaction with the nanopores depends on pore size, arrangement, and thickness of the oxide layer [14].

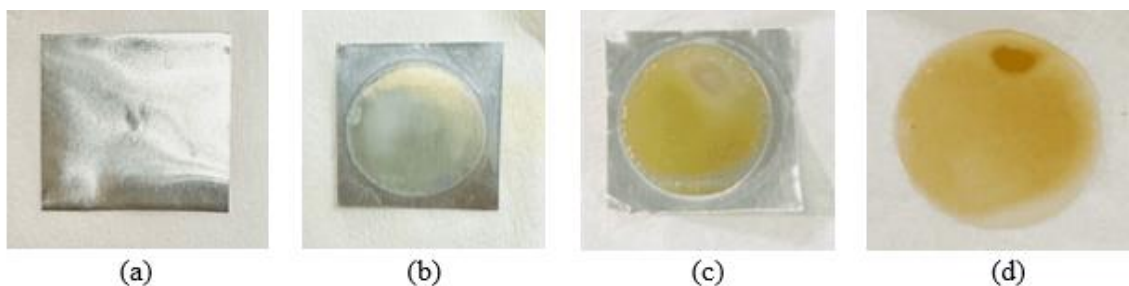


Figure 1. Photograph images of (a) pretreated Al foil and the mAAO after (b) first anodization, (c) second anodization and (d) detachment of unreacted aluminum foil.

Mohammed *et al.* [15] reported that anodization in an acidic environment with an appropriate electrolyte produces self-ordered pores arranged in a closely packed hexagonal lattice. For obtaining a free-standing template, the Al surface was cleaned by sonication in acetone to remove any presence of organic or other contaminant [5], as depicted in **Figure 2 (a)**. The initial oxide film on the aluminum surface is transformed into a thicker oxide layer, known as a planar barrier-type film, during the AAO template production or first anodization process. The formation of random fractures in the outer regions of the barrier oxide layer leads to the development of a porous oxide layer (**Figure 2(b)**) [15]. These cracks expand, creating distinct pathways and it was removed

leading in the formation of a pret textured Al surface (**Figure 2(c)**). A second anodization was performed until a steady-state pore structure is achieved as shown in **Figure 2(d)** followed by the detachment of underlying Al substrate (**Figure 2(e)**). Once this steady state is reached, the bottom pores of the mAAO was opened completing the process (**Figure 2(f)**). Zaraska *et al.* [16] emphasized the necessity of opening or widening these pores because the prepared AAO typically retains closed pore bottoms due to the continuous barrier layer that remains after removing the aluminum substrate. This results from the prolonged interaction between the oxide and the acidic electrolyte, along with the enhanced dissolution of aluminum oxide under the influence of the electric field.

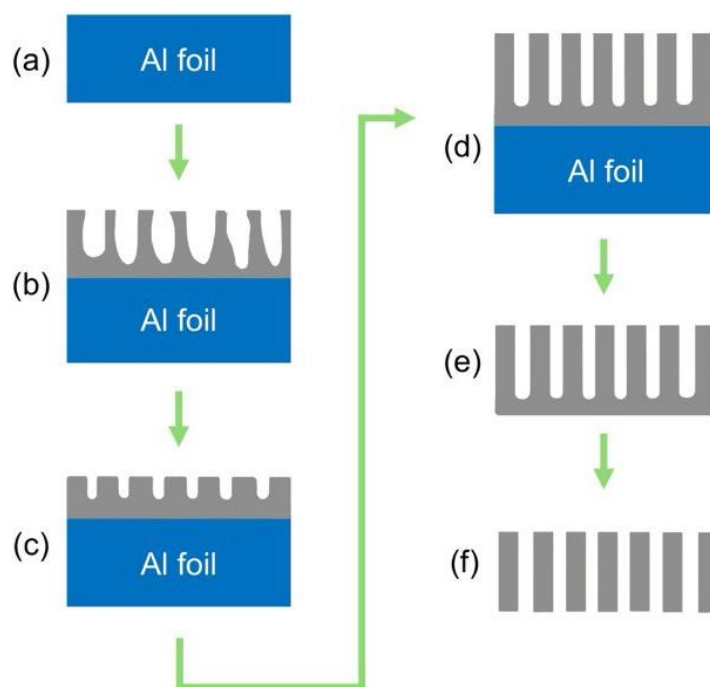


Figure 2. Schematic of formation free-standing AAO. (a) Al surface after pretreatment, (b) first anodization, (c) removal of oxide layer, (d) second anodization, (e) detachment of underlying Al substrate, (f) free-standing AAO.

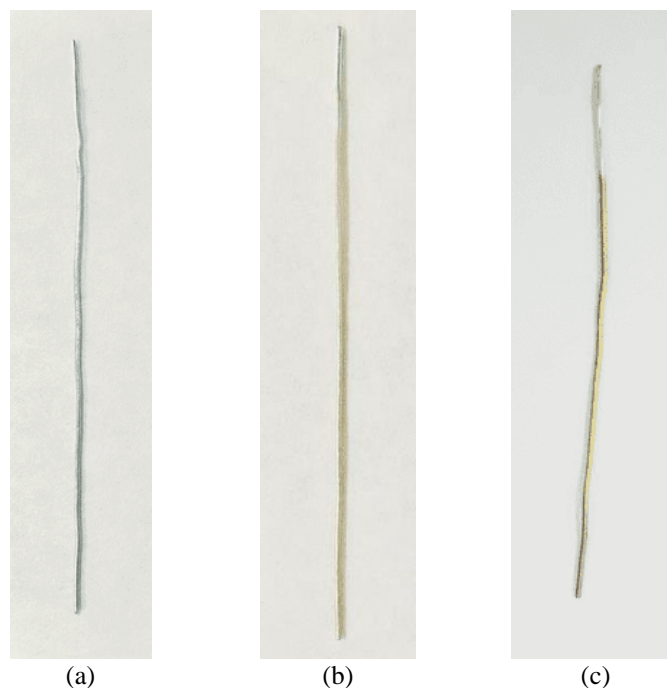


Figure 3. Photograph image of (a) pretreated Al wire and the wAAO after (b) first anodization, and (c) second anodization.

AAO Wire (wAAO)

Figure 3 illustrates the anodic aluminum oxide wire (wAAO) fabricated from pretreated aluminum wire in **Figure 3(a)**, following the electrochemical anodization process outlined by Rajeev *et al.* [10]. The aluminum wire underwent a two-step electrochemical anodization procedure under the same conditions applied to aluminum foil. During the first anodization step, the wire developed a pale brown color, indicating successful anodization, as shown in **Figure 3(b)**. This color change is attributed to the interaction between aluminum ions (Al^{3+}) and the oxalate anions ($\text{C}_2\text{O}_4^{2-}$) present in oxalic acid. Following anodization, the oxidized layer on the aluminum wire surface was removed through an etching process using phosphochromic acid ($\text{H}_3\text{PO}_4\cdot\text{CrO}_3$). Unlike the conditions used for aluminum foil, the etching of the aluminum wire was conducted at 80°C for two hours, as depicted in **Figure 3(c)**. Higher temperature was necessary to enhance the oxide layer's removal rate while preserving the aluminum wire's mechanical integrity.

Surface Modification of mAAO and wAAO

The surface of the mAAO was further modified by hydroxylation using hydrogen peroxide (H_2O_2), followed by silanization with 3-aminopropyl-triethoxysilane

(APTES) solution. During the hydroxylation step, H_2O_2 interacted with the mAAO surface, generating hydroxylated mAAO (mAAO-OH) through the release of hydroxyl ions from the dissociation of hydrogen peroxide. This process introduced hydroxyl groups onto the mAAO surface, facilitating subsequent modifications. Zulkifli *et al.* [5] stated these hydroxyl groups enhance covalent bonding during silanization by creating a high density of reactive sites. In the silanization step, the APTES solution altered the mAAO surface, resulting in the formation of mAAO-OH-Si, where the silicon (Si) element covalently binds to the AAO-OH surface. This reaction introduces amino terminal groups, which are crucial for interacting with gold nanoparticles, playing a key role in achieving optimal nanoparticle coverage and stabilizing the gold nanoparticles [5]. Silanization is an efficient chemical modification technique for enhancing the wettability and adsorption properties of AAO [17].

Structural characterization of bare AAO, hydroxylated AAO (AAO-OH), and silanized AAO (AAO-OH-Si) in both membranes and wires was performed using Fourier Transform Infrared Spectroscopy (FTIR). **Figure 4** displays the FTIR spectra for (a) bare mAAO, (b) hydroxylated mAAO (AAO-OH), and (c) mAAO-OH-Si.

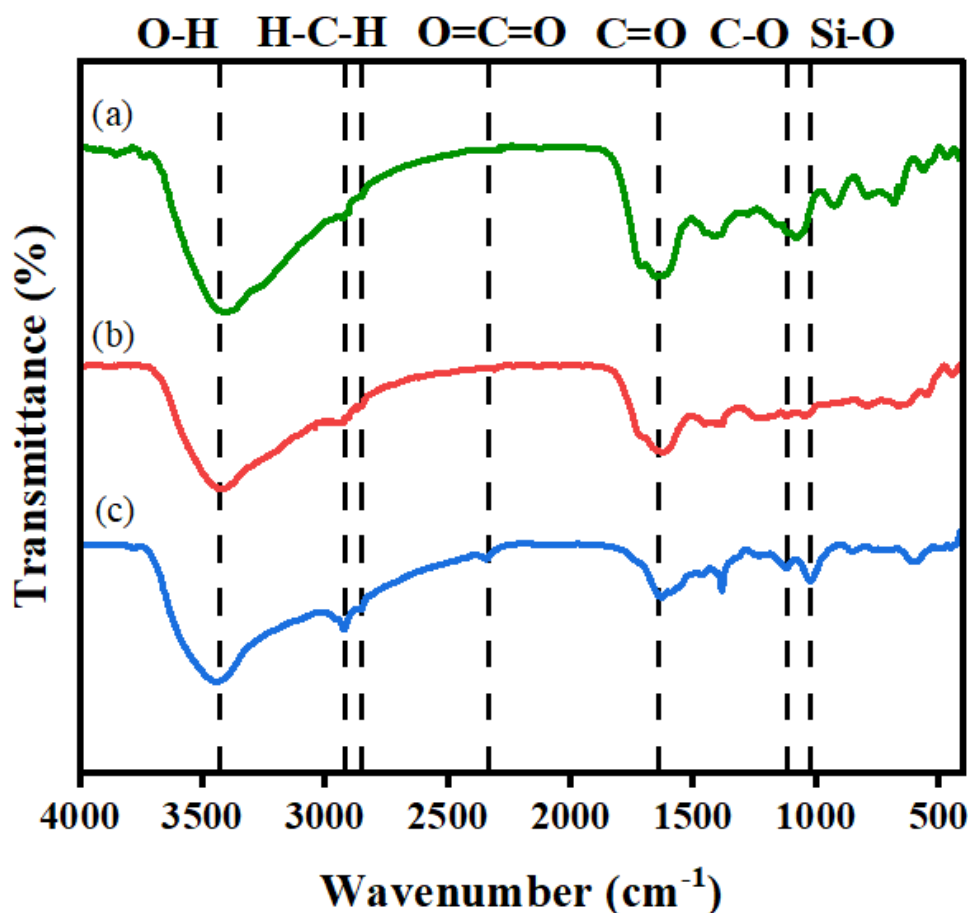


Figure 4. FTIR spectra of (a) bare mAAO (b) mAAO-OH, (c) mAAO-OH-Si.

For bare mAAO, three prominent peaks were observed at 3403 cm^{-1} , 1666 cm^{-1} , and 1122 cm^{-1} , corresponding to O-H, C=O, and C-O stretching functional groups, respectively. These peaks indicate the formation of an oxide layer during the anodization of aluminum foil, with the broad O-H peak confirming the presence of hydroxyl groups. The O-H peak is likely present due to reactions occurring during the pore-widening process in an aqueous solution [18]. The carbonyl (C=O) and C-O stretching peaks further confirm the oxidation of carboxylic acid (COOH) groups on the AAO surface. According to Chung *et al.* [19] these absorption peaks (O-H and C-O) are associated with the interaction of oxalate anions ($\text{C}_2\text{O}_4^{2-}$) with the Al foil surface during anodization. These anions are integrated into the AAO structure at the interface between oxide and electrolyte, which are located close to the surfaces. Therefore, they can be detected on the AAO surfaces by infrared spectroscopy. Following hydroxylation, the peaks shift slightly to 3444 cm^{-1} , 1657 cm^{-1} , and 1124 cm^{-1} indicating the continued presence of O-H, C=O, and C-O groups in the mAAO-OH sample.

In mAAO-OH-Si, additional peaks appear at 3453 cm^{-1} (O-H stretching), 2852 cm^{-1} and 2922 cm^{-1} (CH_2), 2342 cm^{-1} (O=C=O stretching), 1655 cm^{-1} (C=O), 1125 cm^{-1} (C-O stretching) and 1021 cm^{-1} (Si-O). The Si-O peak at 1021 cm^{-1} suggests successful surface modification through silanization, as indicated by the sharp Si-O stretching vibration. Furthermore, the symmetric and antisymmetric of CH_2 vibration bands at 2852 cm^{-1} and 2922 cm^{-1} corresponds to the successful chemical modification of APTES on the hydroxylated AAO surface [5,20-22]. The O=C=O (CO_2) vibration band at 2342 cm^{-1} represents carbon dioxide (CO_2) molecules resulting from the decomposition of oxalate species. The presence of physisorbed CO_2 , loosely bound to the surface, is likely due to CO_2 molecules residing within the cell wall's closed micropores or voids [21,23]. Overall, the hydroxylation and silanization processes introduced pronounced peaks for O-H, C=O, C-O, Si-O and H-C-H groups, indicating an enhancement in the surface properties of AAO. **Table 1** provides a summary of the bonds present and their corresponding wavenumbers for bare mAAO, mAAO-OH, and mAAO-OH-Si in membrane form.

Table 1. IR data of AAO membrane for bare mAAO, mAAO-OH and mAAO-OH-Si.

Nanoporous AAO	Type of vibration	Wavenumber (cm ⁻¹)	References
Bare mAAO	O-H stretching	3403	[5,18,19,24]
	C=O	1666	
	C-O stretching	1122	
mAAO-OH	O-H stretching	3444	[6,19,24]
	C=O	1657	
	C-O	1124	
mAAO-OH-Si	O-H stretching	3453	[6,18,19,21-24]
	H-C-H (CH ₂)	2852, 2922	
	O=C=O (CO ₂) stretching	2342	
	C=O	1655	
	C-O stretching	1125	
	Si-O	1021	

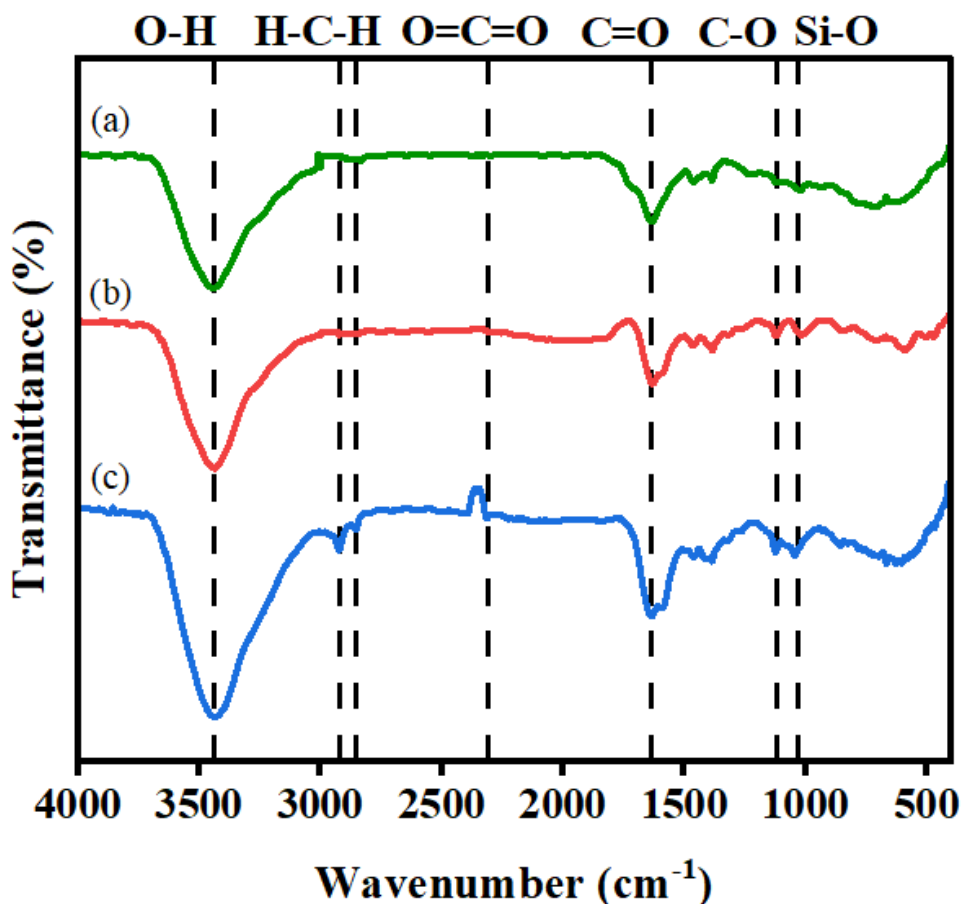


Figure 5. FTIR spectra of (a) bare wAAO (b) wAAO-OH, (c) wAAO-OH-Si.

Table 2. IR data of AAO wire for bare wAAO, wAAO-OH and wAAO-OH-Si.

Nanoporous AAO	Type of vibration	Wavenumber (cm ⁻¹)	References
Bare wAAO	O-H stretching	3442	[18,19,24]
	C=O	1637	
	C-O stretching	1125	
wAAO-OH	O-H stretching	3436	[19,24]
	C=O	1630	
	C-O	1121	
wAAO-OH-Si	O-H stretching	3434	[6,18,19,21-24]
	H-C-H (CH ₂)	2851, 2920	
	O=C=O (CO ₂) stretching	2316	
	C=O	1631	
	C-O stretching	1123	
	Si-O	1045	

Figure 5 shows the FTIR spectra for (a) bare wAAO, (b) hydroxylated wAAO (AAO-OH), and (c) silanized wAAO (wAAO-OH-Si). The formation of an oxide layer on bare wAAO is evident at wavenumber 3442 cm⁻¹, 1637 cm⁻¹, and 1125 cm⁻¹, corresponding to O-H, C=O, and C-O stretching functional groups, respectively. Following hydroxylation, these peaks shifted slightly to 3436 cm⁻¹, 1630 cm⁻¹, and 1121 cm⁻¹ in wAAO-OH, indicating the continued presence of O-H, C=O, and C-O groups. In the spectrum of wAAO-OH-Si, additional peaks appeared at 3434 cm⁻¹ (O-H stretching), 2851 cm⁻¹ and 2920 cm⁻¹ (CH₂), 2316 cm⁻¹ (O=C=O stretching), 1631 cm⁻¹ (C=O), 1123 cm⁻¹ (C-O stretching) and 1045 cm⁻¹ (Si-O). The Si-O peak at 1045 cm⁻¹ indicates successful silanization wAAO-OH, as evidenced by the sharp Si-O stretching vibration. Additionally, the O=C=O (CO₂) vibration band at 2316 cm⁻¹ corresponds to carbon dioxide (CO₂) molecules, likely a byproduct of oxalate species decomposition. The silanization of the AAO surface also was confirmed due to the presence of two CH₂ vibration bonds at 2851 cm⁻¹ and 2920 cm⁻¹ which attributed to the binding of alkyl silane on the AAO surface [5,20]. **Table 2** summarizes the types of bonds, and their corresponding wavenumbers observed in bare wAAO, wAAO-OH, and wAAO-OH-Si.

Gold on AAO Membrane (Au/mAAO) and AAO Wire (Au/wAAO)

Gold Chloride Precursor

Initially, the gold solution was heated to 80 °C, exhibiting a bright yellow color with a pH of 2, attributed to the presence of tetrachloroaurate ion complexes [AuCl₄]⁻. The solution's pH was then adjusted to 8 by gradually adding 0.25 M sodium hydroxide (NaOH). As the pH increased, the solution transitioned from bright yellow to light yellow and eventually turned colorless at pH 8. As described by Moreau and Bond [25], the hydrolysis of [AuCl₄]⁻ ions with increasing pH leads to the formation of various gold complex species such as [AuCl₃(OH)]⁻, AuCl₃(H₂O), [AuCl₂(OH₂)]⁻, [AuCl(OH)₃]⁻, and [Au(OH)₄]⁻. These dissociated ions are generated through three key processes: displacement of chloride ions (Cl⁻), where Cl⁻ in the complex anion is replaced by water molecules, creating neutral species as represented in equations (1) and (3); loss of a proton from neutral hydrated ions as shown in equations (2) and (4); and hydrolysis, where Cl⁻ ions are replaced by hydroxyl ions (OH⁻), as indicated in equations (5) and (6).

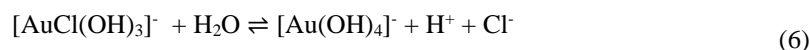
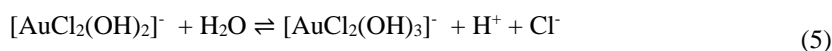
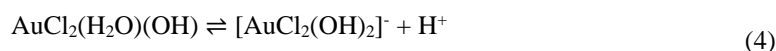
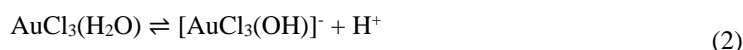
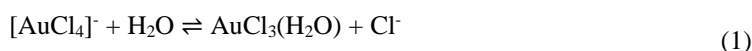




Figure 6. Image of (a) Au/mAAO and (b) Au/wAAO.

Yazid *et al.* [11] reported that adjusting the pH of Au precursor solution generates several negatively charged Au species, such as $\text{AuCl}_x(\text{OH})_{4-x}$ ($x = 0-3$). These anionic species can readily bond with amino group (NH_3^+) on the AAO surface through electrostatic adsorption, enhancing Au attachment to AAO. This pH-driven mechanism facilitates Au immobilization, resulting in functionalized AAO surface for catalytic reduction.

Characterization of Au/mAAO and Au/wAAO

Figure 6 represents the appearance of gold (Au) deposited on anodic aluminum oxide (AAO) in both membrane and wire forms after 4 hours of calcination. The Au/mAAO exhibits a color gradient from slightly red to purple while the AAO wire (Au/wAAO) appears black depending on the initial color of the synthesized Au solution. Yazid *et al.* [11] stated that the calcination process is required as the last stage in the deposition-precipitation (DP) process to eliminate any remaining chloride ions (Cl^-) from the Au precursor and reduce Au^{3+} to Au^0 . Additionally, the annealing of Au nanoparticles (Au NPs) at 400°C following deposition, washing, and drying steps enhances their stability, resulting in more robust Au NPs.

The distinct color differences between Au/mAAO and Au/wAAO after calcination can be attributed to interference phenomena and surface plasmon resonance (SPR) effects, as described by Ruiz-Clavijo *et al.* [13]. The slight red-to-purple hue observed in Au/mAAO arises from the interference

effect caused by the periodic arrangement of nanopores where constructive interference at specific wavelengths when light interacts with the nanoporous structure. In contrast, the black color of Au/wAAO is due to a shift in SPR. On the surface of gold nanoparticles, plasmons, or collective oscillations of conduction electrons, occur at specific wavelengths. During the calcination process, the SPR shifts to a longer wavelength in the infrared region, leading to the absorption of visible light, and the absence of reflection resulting in the black appearance of Au/wAAO [13]. The impact of gold attachment on the chemical functionality of the AAO in both membrane and wire forms was further investigated using FTIR spectroscopy.

Figure 7 presents the FTIR spectra of Au/mAAO compared with mAAO-OH-Si. A distinct peak at 3444 cm^{-1} , corresponding to the O-H stretching functional group, closely matches the peak at 3453 cm^{-1} observed in mAAO-OH-Si. The attachment of gold to the AAO surface caused these peaks to become sharper and broader peaks compared to mAAO-OH-Si, indicating successful chemical modification of the AAO surface following gold immobilization. Additionally, other characteristic peak bands, such as C=O and C-O exhibited similar patterns in Au/mAAO as those observed in mAAO-OH-Si. The peak bands of (H-C-H) CH_2 , C-O and Si-O, exhibited similar patterns in Au/mAAO as those observed in mAAO-OH-Si. Sharper C=O and O=C=O (CO_2) peaks were also observed in the Au/mAAO indicating that silanized AAO surface was successfully attached with immobilized gold nanoparticles.

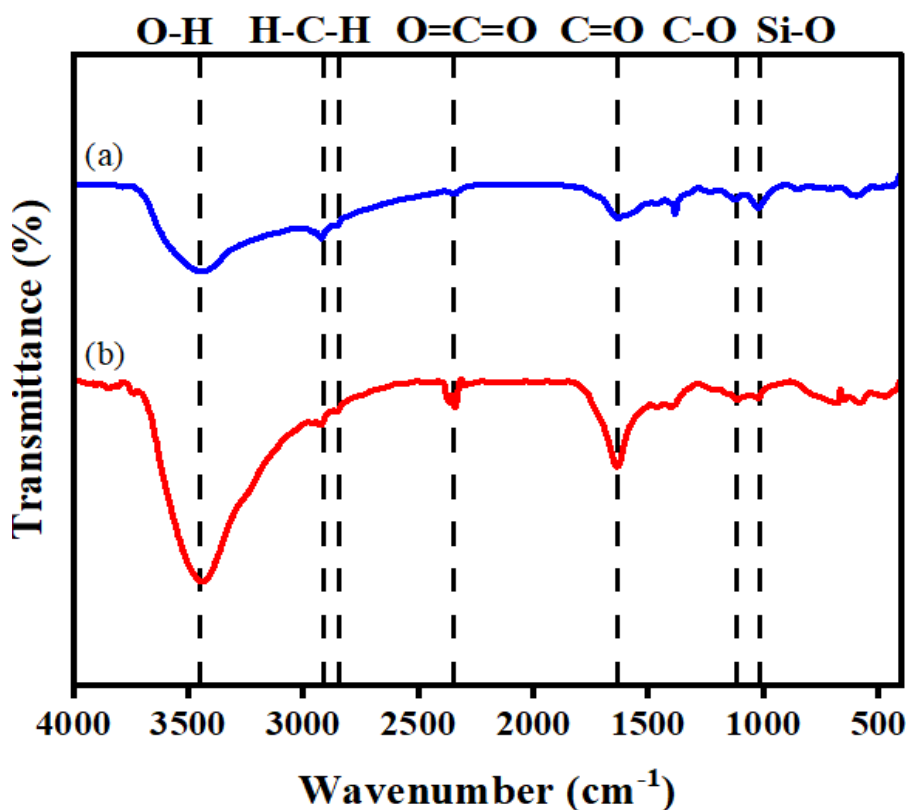


Figure 7. FTIR spectra of (a) mAAO-OH-Si and (b) Au/mAAO.

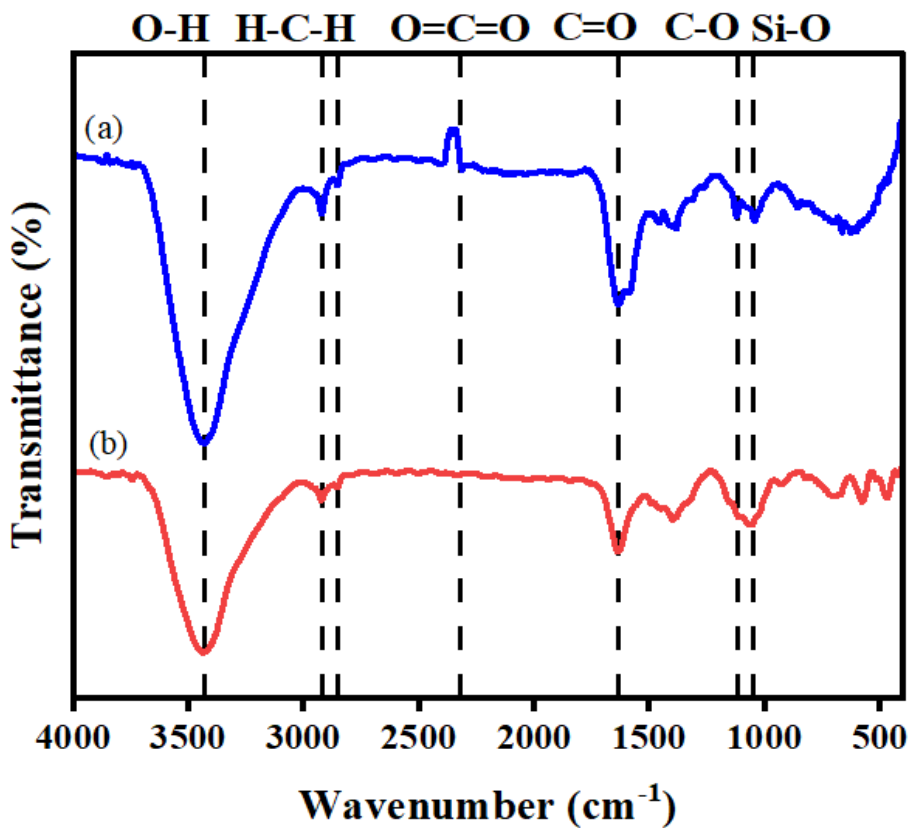


Figure 8. FTIR spectra of (a) wAAO-OH-Si and (b) Au/wAAO.

Figure 8 presents the FTIR spectra comparing Au/wAAO with wAAO-OH-Si. The spectra reveal a distinct peak at 3438 cm^{-1} , corresponding to the O-H stretching functional group, which closely aligns with the 3434 cm^{-1} peak observed for wAAO-OH-Si in wire form. The data suggests that the attachment of gold to the AAO surface resulted in sharper and broader peaks compared to wAAO-OH-Si, indicating successful chemical modification of the AAO after Au attachment. Other characteristic peaks, including (H-C-H) CH_2 , C-O, C=O and SiO, displayed similar patterns in Au/wAAO as those in wAAO-OH-Si. The CH_2 bands correspond to the alkyl silane group derived from the APTES solution, which is covalently bonded on the AAO surface [5]. The post-functionalization of silanized wAAO is essential for modifying the terminal functional groups, enabling the attachment of nanoscale species like Au [26,27]. In contrast, O=C=O (CO_2) peak was only discovered in wAAO-OH-Si with the wavenumber of 2316 cm^{-1} . Jani *et al.* [21] and Haneda *et al.* [28] highlighted the presence of O=C=O (CO_2) peak due to the adsorption of environmental CO_2 onto the functionalized AAO surface. This CO_2 species interacts with the basic hydroxyl groups on the

AAO surface. Hence, these findings confirm that both Au/mAAO and Au/wAAO demonstrated successful reduction of the gold precursor from Au^{3+} to Au^0 , signifying effective gold attachment to the AAO structures. The observed shifts in peaks after gold deposition, compared to the AAO-OH-Si state in both membrane and wire forms, provide strong evidence of the stable incorporation of gold onto the modified AAO surfaces.

Figures 9(a) and (b) present the XRD patterns for Au/mAAO and Au/wAAO, respectively. Both samples exhibit distinct diffraction peaks characteristic of Au at 2θ values of 38.26° , 44.48° , 64.75° , and 77.65° , which can be indexed to the (111), (200), (220), and (311) crystal planes of the Au phase, respectively, according to ICDD reference no. 01-089-3697 [11,29]. A broad diffraction pattern observed below 30° corresponds to the amorphous structure of AAO, further confirming the amorphous nature of the support material [30]. These well-defined diffraction peaks from Au confirm the successful deposition of nanocrystalline Au onto the amorphous AAO surface.

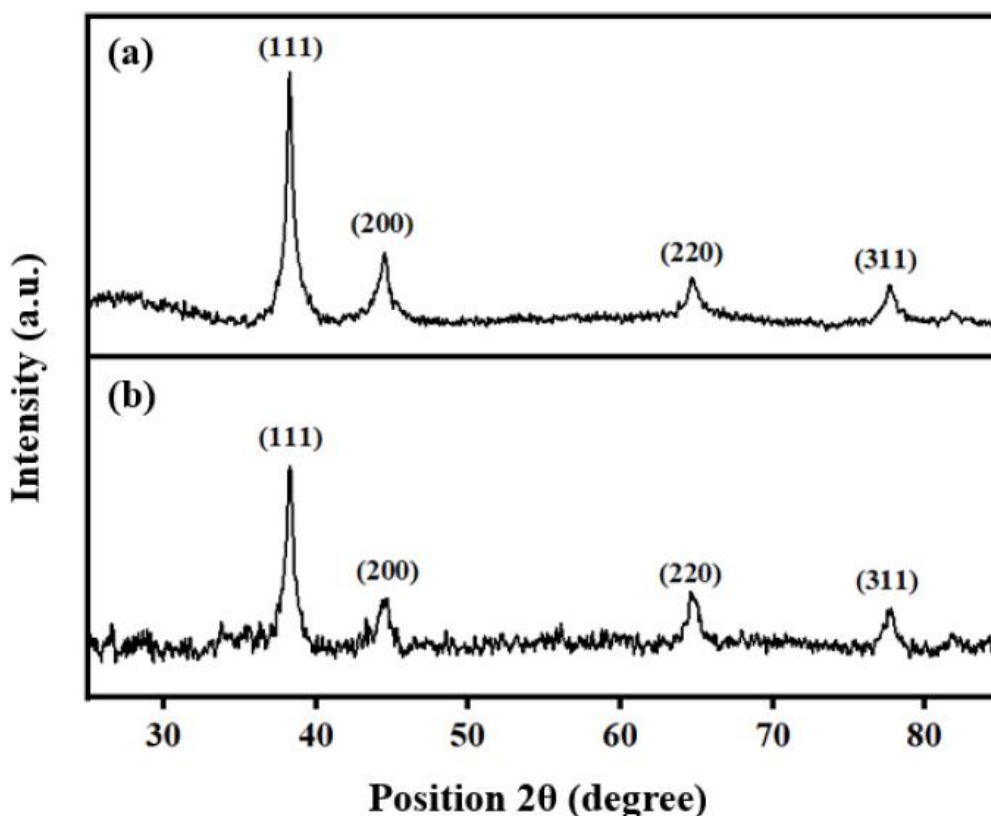


Figure 9. X-ray diffraction pattern for (a) Au/mAAO and (b) Au/wAAO.

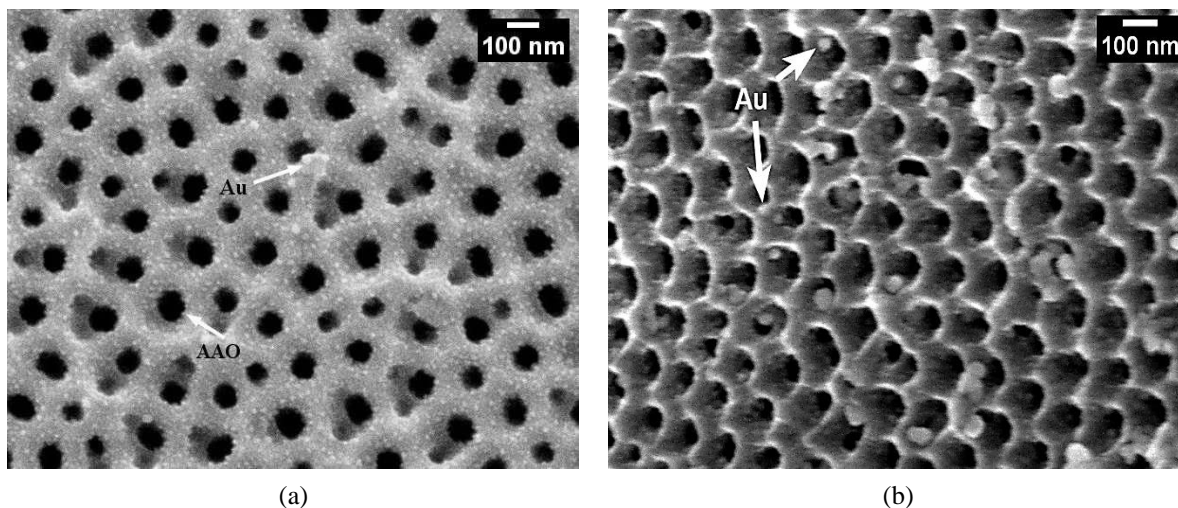


Figure 10. FE-SEM images of (a) Au/mAAO and (b) Au/wAAO.

Furthermore, Field Emission Scanning Electron Microscopy (FE-SEM) at 100,000 \times magnification was employed to determine the surface morphology and structure of the Au/mAAO and Au/wAAO. Besides, the images from the FE-SEM analysis can be used to determine the average size of Au nanoparticles deposited on the AAO surface. **Figure 10(a)** and **(b)** show the FE-SEM images of Au/mAAO and Au/wAAO, respectively. Both images display closely packed, regular-shaped pores, which are characteristic of AAO. According to Sundararajan *et al.* [31], AAO typically exhibits highly organized porous structures, often displaying hexagonal or honeycomb patterns as a result of the controlled oxidation process during electrochemical anodization. The pores of wire AAO are slightly convex due to the curvature of the wire's surface, whereas in membrane AAO, the pores are more uniform and flatter, resulting from the flat surface of the membrane [32]. Additionally, the Au NPs are visible in the images as individual nanoparticles scattered on the AAO surface near the pore regions with some clustering together to form aggregates. ImageJ software was utilized to measure the average pore size of AAO and the size of Au NPs yielding values of 76.75 ± 11.29 nm and 16.03 ± 5.54 nm for Au/mAAO while 74.97 ± 10.49 nm and 18.43 ± 11.16 nm for Au/wAAO, respectively. A slightly larger size of Au nanoparticles in Au/wAAO is observed, with a higher standard deviation (SD) of 11.16, indicating a broader Au nanoparticle size distribution compared to Au/mAAO, which has an SD of 5.54. The quantification of Au in Au/mAAO and Au/wAAO are 0.88 wt.% and 0.92 wt.%, respectively.

Catalytic Study

Catalytic Reduction of *p*-NP over Au/mAAO and Au/wAAO

p-Nitrophenol (*p*-NP) also known as 4-Nitrophenol or 4-hydroxynitrobenzene, is a phenolic compound that appears light-yellow aqueous solution. According to Kadam *et al.* [33], *p*-NP has a characteristic absorption peak at 317 nm, which represents its maximum absorbance value (λ_{\max}). However, upon the addition of sodium borohydride (NaBH_4), the *p*-NP solution turns a deeper yellow due to the interaction with the alkaline medium causing the absorption band to shift from 317 nm to 400 nm. This shift is attributed to the formation of *p*-nitrophenolate anions. This change can be explained by the electron transition from the phenol ring ($\pi \rightarrow \pi^*$) to the lone pair of electrons on the oxygen and nitrogen atoms ($n \rightarrow \pi^*$) [34]. The reduction of *p*-NP leads to the formation of *p*-aminophenol (*p*-AP) an organic compound and valuable intermediate known for its lower toxicity. In the presence of gold nanoparticles (Au NPs) supported on AAO along with an excess of NaBH_4 as the hydrogen source, the *p*-nitrophenolate ion is efficiently converted to *p*-AP, as illustrated in the inset image of **Figure 11**. This process causes the absorption peak at 400 nm (*p*-nitrophenolate ion) to shift to approximately 300 nm corresponding to the *p*-aminophenol peak, as depicted in **Figure 11**. UV-Vis spectroscopy has been utilized to monitor this transformation showing a significant decrease in the *p*-NP absorption peaks over time as it reduced to *p*-AP.

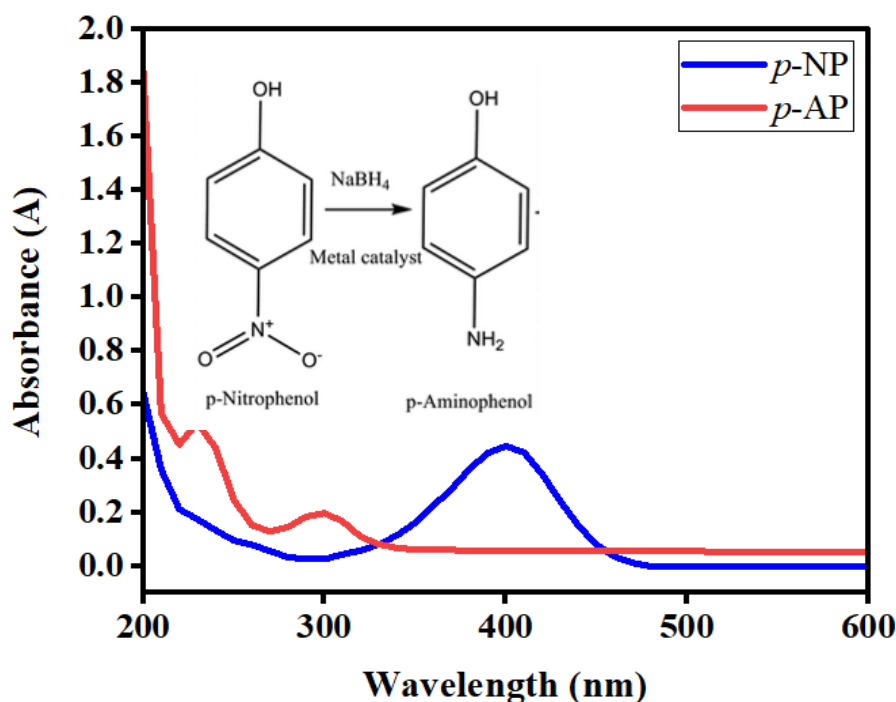


Figure 11. UV-Vis spectra of (a) *p*-nitrophenolate ion (b) *p*-AP. Inset is the chemical transformation of *p*-NP to *p*-AP in the presence of gold catalysts.

Therefore, the catalytic activity of Au/AAO catalyst for both membrane and wire forms was investigated using the reduction of *p*-NP to *p*-AP as a model reaction with excess sodium borohydride (NaBH_4) serving as the hydrogen source. To ensure pseudo-first-order kinetics and a high reaction rate, an excess of NaBH_4 and a minimal quantity of catalyst were used, following the approach outlined by Swathy *et al.* [35]. The progress catalytic reduction was monitored via UV-Vis spectroscopy, which showed a notable decrease in the *p*-nitrophenolate ion absorption

peak at 400 nm and the appearance of a *p*-AP absorption peak at 300 nm. The conversion was further confirmed by the color change of the *p*-NP solution from yellow to colorless as shown in **Figure 12**. According to Wang *et al.* [36], the catalytic reduction of the *p*-NP solution clearly showed that the yellow color of the solution faded over time in the presence of Au NPs. The Au NPs play a crucial role by lowering the activation energy barrier, enabling efficient electron transfer from the borohydride anion (BH_4^-) to the *p*-nitrophenolate, thereby promoting the reduction of *p*-NP to *p*-AP.

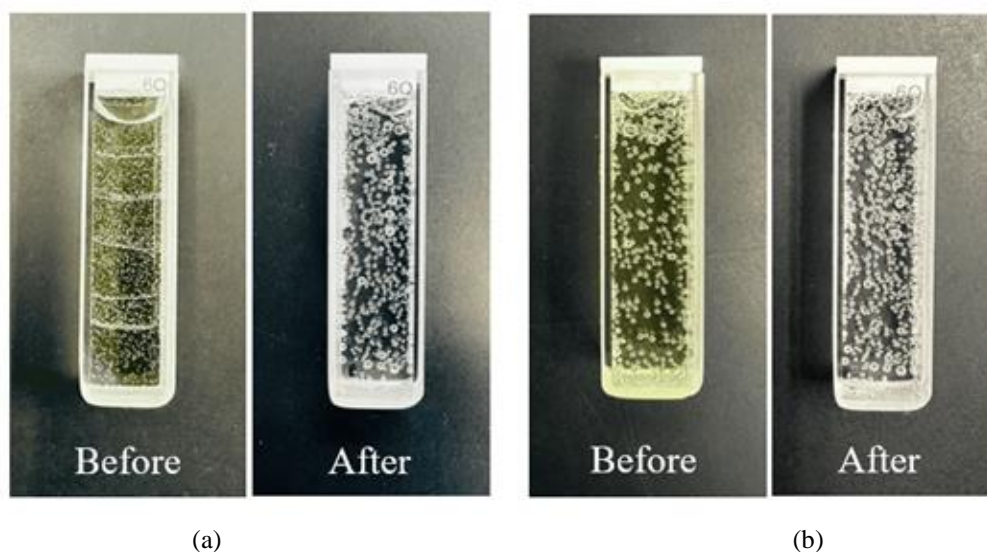


Figure 12. Photograph of *p*-NP solution before and after catalytic reduction for (a) Au/mAAO and (b) Au/wAAO.

The reduction of *p*-NP follows pseudo-first-order kinetics, and the rate constant value (*k*) was determined from the graph of $\ln [A/A_0]$ against the reaction time in seconds. The linear fit of this graph confirmed that the reaction adheres to the first-order kinetic laws as described by Zulkifli *et al.* [5]. The rate constant value (*k*) was calculated using the equation $\ln [A/A_0] = kt$ where *k* is the rate constant, *t* represents the irradiation time, *A* is the concentration at time *t*, and *A*₀ is the concentration at *t*=0. Additionally, Swathy *et al.* [35] stated that the slope of the linear regression fit can be used to obtain the rate constant confirming the pseudo-first-order kinetics of the reaction.

Figure 13 presents a plot of $\ln [A/A_0]$ versus time plot for both the Au/mAAO and Au/wAAO catalysts. The data reveals that Au/mAAO has a significant (*k*) value of $4.24 \times 10^{-3} \text{ s}^{-1}$ compared to Au/wAAO, which has a *k* value of $4.31 \times 10^{-4} \text{ s}^{-1}$. Several factors contribute to the superior performance of Au/mAAO including its larger surface area and more uniform pore structure. As highlighted by Huang *et al.* [37], AAO membranes (mAAO) feature highly hexagonal porous structures, resulting in a large surface area that provides more active sites for the deposition of gold nanoparticles deposition. These active sites are crucial for catalyzing the reduction of *p*-nitrophenol. The increased surface area of mAAO enhances the adsorption of reactant molecules, improving interaction between the catalyst and the

reactant. Furthermore, the uniform distribution of Au nanoparticles within the mAAO pores facilitates better accessibility to catalytic sites, significantly enhancing overall performance. Ruiz-Clavijo *et al.* [13] emphasized that a well-distributed array of gold nanoparticles within the mAAO pores ensures a higher number of available active sites, thus improving catalytic efficiency.

In addition, the size of supported Au NPs plays a pivotal role in determining the catalytic efficiency for *p*-nitrophenol reduction [38,39]. According to Lin *et al.* [39], smaller Au NPs exhibit enhanced catalytic activity due to their higher surface area-to-volume ratio, providing more active sites for the reaction and accelerating the reduction rate. Hence, it was proven that Au/mAAO was the best catalytic performance, having a smaller Au NPs size in comparison with Au/wAAO. Despite Au/wAAO having higher gold loading, the larger Au NPs led to particle aggregation, reduced active surface area, and diminished overall catalytic efficiency [40]. Conversely, the one-dimensional structure of Au/AAO wire (wAAO) leads to non-uniform distribution and potential agglomeration of gold nanoparticles. This non-uniform distribution reduces the number of accessible active sites and lowers overall catalytic efficiency as highlighted by Zhou and Nonnenmann [3]. Therefore, the higher *k* value observed in Au/mAAO reflects a faster reaction rate and a more efficient reduction process for *p*-nitrophenol compared to Au/wAAO.

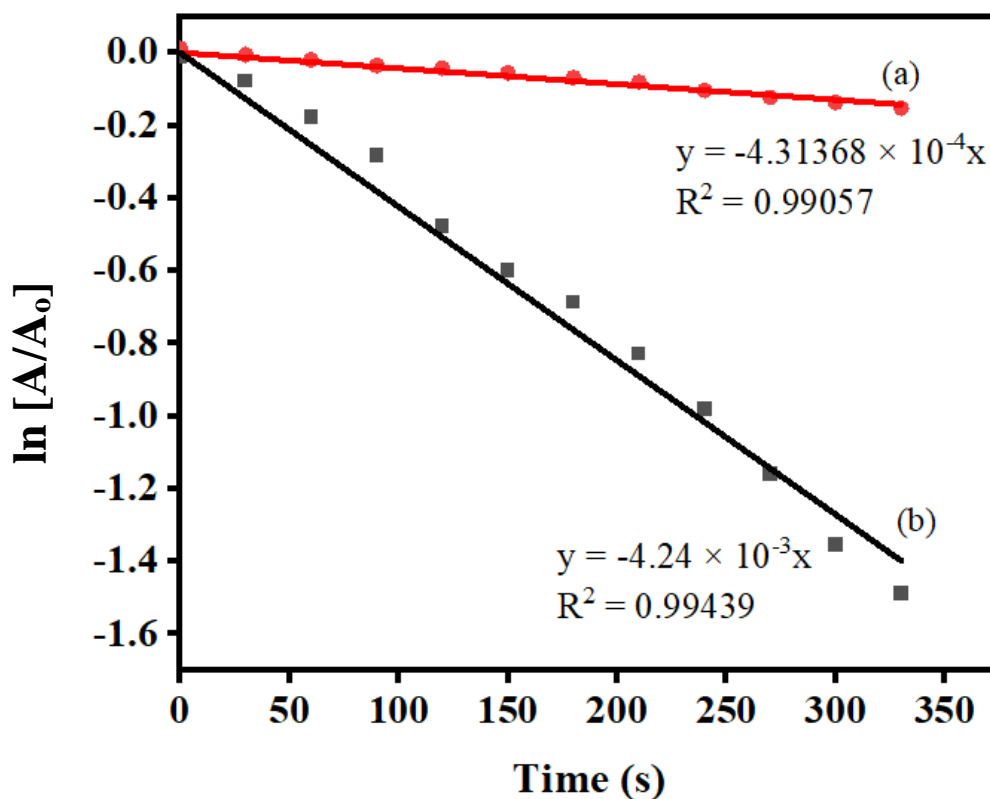


Figure 13. Graph of $\ln [A/A_0]$ vs time (s) for *p*-NP reduction (a) Au/wAAO (b) Au/mAAO.

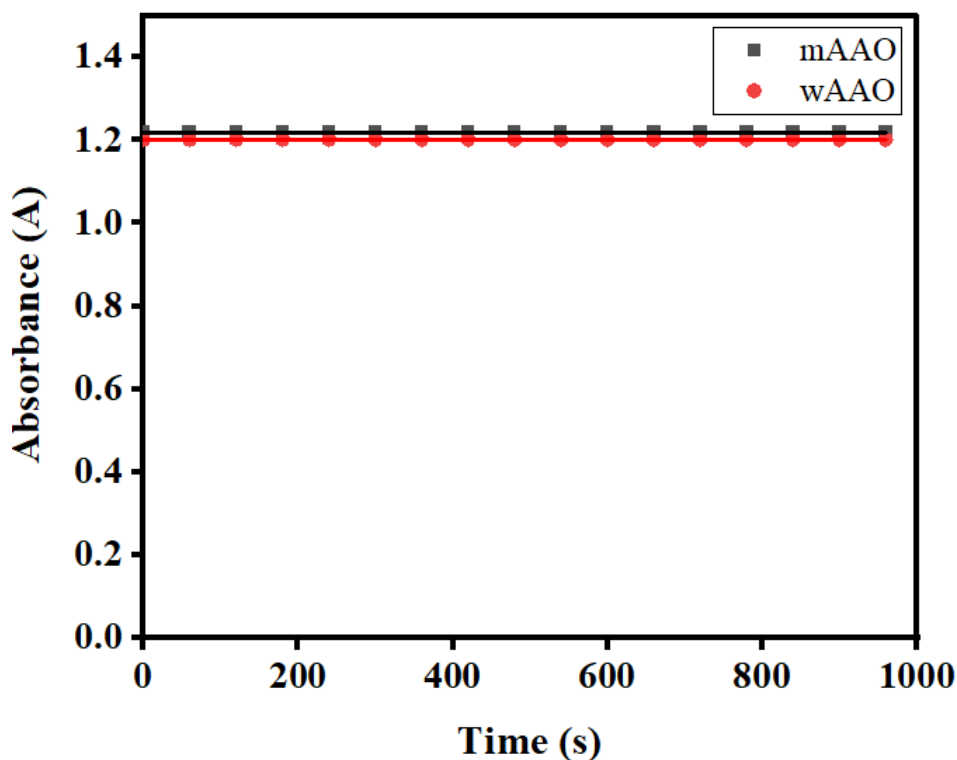


Figure 14. Graph of absorbance vs time (s) for *p*-NP reduction (a) mAAO (b) wAAO.

A controlled study was conducted on the critical role of the Au supported by AAO for the catalytic reduction of *p*-NP. A UV-Vis characterization was employed to determine whether Au is responsible for the observed catalytic activity as illustrated in **Figure 14**. The UV spectra shows that no reduction process occurs in the presence of excess NaBH_4 alone, as indicated by the plateau absorbance line. The presence of Au NPs facilitates the activation of the nitro group in *p*-NP by enhancing the electron transfer, enabling the reduction to proceed and yielding the desired product *p*-AP [41,42].

CONCLUSION

In conclusion, the AAO membrane and wire were successfully fabricated using two-step electrochemical anodization techniques of Al foil and wire respectively. Surface modification through hydroxylation and silanization yielded bare AAO, hydroxylated AAO (AAO-OH), and AAO-OH-Si. FTIR analysis in the wavenumber range $4000\text{--}400\text{ cm}^{-1}$ confirmed the presence of functional groups like O-H, C-O, C=O, Si-O, and O=C=O in both mAAO and wAAO. Gold nanoparticles were deposited onto the AAO surfaces using the deposition-precipitation technique at pH 8 and FTIR characterization showed peak shifts, indicating the successful attachment of gold compared to unmodified support. The calcination process resulted in distinct colors before and after calcination: slightly red to purple for Au/mAAO and black for Au/wAAO. UV-Vis spectroscopy showed that in the reduction of *p*-NP, Au/mAAO demonstrated a higher

catalytic activity ($k = 4.24 \times 10^{-3}\text{ s}^{-1}$) compared to Au/wAAO ($k = 4.31 \times 10^{-4}\text{ s}^{-1}$). The highest value achieved in this research are with Au loading of 0.88 wt% having $76.75 \pm 11.29\text{ nm}$ (average pore size) nm and $16.03 \pm 5.54\text{ nm}$ (Au NPs size). For Au/wAAO, the observed Au loading is 0.92 wt% with average pore size and nanoparticle size of $74.97 \pm 10.49\text{ nm}$ and $18.43 \pm 11.16\text{ nm}$. This research confirms that Au/mAAO exhibits superior catalytic activity. Future research should explore alternative forms of AAO structures, such as hollow tubes, nanotubes, or nanowires to optimize gold deposition. Additionally, the reusability of Au/AAO catalysts should be assessed to ensure long-term efficacy and validate their theoretical property of being reusable and not consumed during reactions.

ACKNOWLEDGEMENTS

The authors gratefully acknowledge the funding by the Fundamental Research Grant Scheme (FRGS) under the Ministry of Higher Education (KPT) Malaysia with grant No. FRGS/1/2024/STG05/UITM/02/18 and Universiti Teknologi MARA.

REFERENCES

1. Poinern, G. E. J., Ali, N. and Fawcett, D. (2011) Progress in nano-engineered anodic aluminum oxide membrane development. *Materials*, **4**, 487–526.

2. Nehra, M., Dilbaghi, A. N., Singh, V., Singhal, N. K. and Kumar, S. (2020) Highly ordered and crystalline Cu nanowires in anodic aluminum oxide membranes for biomedical applications. *Physica Status Solidi*, **217**, 842–856.
3. Zhou, Z. and Nonnenmann, S. S. (2019) Progress in nanoporous templates: Beyond anodic aluminum oxide and towards functional complex materials. *Materials*, **12**, 2535–2551.
4. Erdogan, P., Yuksel, B. and Birol, Y. (2012) Effect of chemical etching on the morphology of anodic aluminum oxides in the two-step anodization process. *Applied Surface Science*, **258**, 4544–4550.
5. Zulkifli, F. W. A., Yazid, H. and Jani, A. M. M. (2021) Immobilization of carbon nanotubes decorated gold nanoparticles on anodized aluminium oxide (Au-CNTs-AAO) membrane for enhanced catalytic performance. *Materials Chemistry and Physics*, **264**, 124445–124456.
6. Patel, Y., Janusas, G., Palevicius, A. and Vilkauskas, A. (2020) Development of nanoporous AAO membrane for nano filtration using the acoustophoresis method. *Sensors*, **20**, 3833–3850.
7. Alshammari, A. S. (2019) Heterogeneous gold catalysis: from discovery to applications. *Catalysts*, **9**, 402–424.
8. Carabineiro, S. A. (2019) Supported gold nanoparticles as catalysts for the oxidation of alcohols and alkanes. *Frontiers in Chemistry*, **7**, 702–734.
9. Li, Y. G., Quan, X., Hu, C. and Li, C. (2020) Effective catalytic reduction of 4-nitrophenol to 4-aminophenol over etched halloysite nanotubes@ α -Ni(OH)₂. *ACS Applied Energy Materials*, **3**, 4756–4766.
10. Rajeev, G., Melville, E., Cowin, A. J., Prieto-Simon, B. and Voelcker, N. H. (2020) Porous alumina membrane-based electrochemical biosensor for protein biomarker detection in chronic wounds. *Frontiers in Chemistry*, **8**, 155–170.
11. Yazid, H., Hadzir, N. M., Adnan, R. and Jani, A. M. M. (2022) Gold decorated on anodic aluminium oxide and its unique catalytic activity. *Materials Today: Proceedings*, **66**, 4000–4004.
12. Sener, M., Sisman, O. and Kilinc, N. (2023) AAO-Assisted nanoporous platinum films for hydrogen sensor application. *Catalysts*, **13**, 459–470.
13. Ruiz-Clavijo, A., Caballero-Calero, O. and Martín-González, M. (2021) Revisiting anodic alumina templates: From fabrication to applications. *Nanoscale*, **13**, 2227–2265.
14. Choudhari, K., Kulkarni, S. D., Unnikrishnan, V., Sinha, R. K., Santhosh, C. and George, S. D. (2019) Optical characterizations of nanoporous anodic alumina for thickness measurements using interference oscillations. *Nano-Structures & Nano-Objects*, **19**, 354–360.
15. Mohammed, H., Moreno, J. A. and Kosel, J. (2017) Advanced fabrication and characterization of magnetic nanowires. *Magnetism and Magnetic Materials*, **2**, 137–164.
16. Zaraska, L., Sulka, G. D. and Jaskuła, M. (2011) Anodic alumina membranes with defined pore diameters and thicknesses obtained by adjusting the anodizing duration and pore opening/widening time. *Journal of Solid State Electrochemistry*, **15**, 2427–2436.
17. Davoodi, E., Zhianmanesh, M., Montazerian, H., Milani, A. S. and Hoorfar, M. (2020) Nano-porous anodic alumina: Fundamentals and applications in tissue engineering. *Journal of Materials Science: Materials in Medicine*, **31**, 1–16.
18. Sundararajan, M., Subramani, S., Devarajan, M. and Jaafar, M. (2020) Synthesis and analysis of anodic aluminum oxide-nanopore structure on Al substrates for efficient thermal management in electronic packaging. *Journal of Materials Science: Materials in Electronics*, **31**, 9641–9649.
19. Chung, C. -K., Tsai, C., Hsu, C., Kuo, E., Chen, Y. and Chung, I. (2017) Impurity and temperature enhanced growth behaviour of anodic aluminium oxide from AA5052 Al-Mg alloy using hybrid pulse anodization at room temperature. *Corrosion Science*, **125**, 40–47.
20. Kurtan, U. and Baykal, A. (2014) Fabrication and characterization of Fe₃O₄@ APTES@ PAMAM-Ag highly active and recyclable magnetic nanocatalyst: Catalytic reduction of 4-nitrophenol. *Materials Research Bulletin*, **60**, 79–87.
21. Jani, A. M. M., Zhou, J., Nussio, M. R., Losic, D., Shapter, J. G. and Voelcker, N. H. (2008) Pore spanning lipid bilayers on silanised nanoporous alumina membranes. *Smart Materials V, International Society for Optics and Photonics*, 1–11.
22. Szczepanski, V., Vlassioug, I. and Smirnov, S. (2006) Stability of silane modifiers on alumina nanoporous membranes. *Journal of Membrane Science*, **281**, 587–591.
23. Roslyakov, I., Kolesnik, I., Levin, E., Katorova, N., Pestrikov, P., Kardash, T. Y., Solovyov, L. and Napolskii, K. (2020) Annealing induced structural and phase transitions in anodic aluminum oxide

- prepared in oxalic acid electrolyte. *Surface and Coatings Technology*, **381**, 1–30.
24. Xu, D., Zhen, C. and Zhao, H. (2021) Microstructure and photoluminescence properties of anodized aluminum oxide films treated by argon ion. *Ceramics International*, **47**, 14382–14389.
 25. Moreau, F. and Bond, G. C. (2007) Preparation and reactivation of Au/TiO₂ catalysts. *Catalysis Today*, **122**, 260–265.
 26. Ahangaran, F. and Navarchian, A. H. (2020) Recent advances in chemical surface modification of metal oxide nanoparticles with silane coupling agents: A review. *Advances in Colloid and Interface Science*, **286**, 1–20.
 27. Kassaei, M. Z., Masrouei, H. and Movahedi, F. (2011) Sulfamic acid-functionalized magnetic Fe₃O₄ nanoparticles as an efficient and reusable catalyst for one-pot synthesis of α -amino nitriles in water. *Applied Catalysis A: General*, **395**, 28–33.
 28. Haneda, M., Joubert, E., Ménézo, J. -C., Duprez, D., Barbier, J., Bion, N., Daturi, M., Saussey, J., Lavalley, J. -C. and Hamada, H. (2001) Surface characterization of alumina-supported catalysts prepared by sol-gel method. Part II.-Surface reactivity with CO. *Physical Chemistry Chemical Physics*, **3**, 1371–1375.
 29. Xie, J. -F., Li, H. -T., Gao, Q., Wang, H. and Gong, Y. -S. (2018) A convenient and efficient precursor transformation route to well-dispersed, stable, and highly accessible supported Au nanocatalysts with excellent catalytic hydrogenation performances. *RSC Advances*, **8**, 39384–39393.
 30. Roslyakov, I., Shirin, N., Berekchiian, M., Shatalova, T., Garshev, A. and Napolskii, K. (2020) Coarse-grain alpha-alumina films with highly ordered porous structure. *Microporous and Mesoporous Materials*, **294**, 109–132.
 31. Sundararajan, M., Devarajan, M. and Jaafar, M. (2020) Investigation of surface and mechanical properties of anodic aluminium oxide (AAO) developed on Al substrate for an electronic package enclosure. *Surface and Coatings Technology*, **401**, 1–45.
 32. Mahmud, A. H., Salahuddin, N. M., Jani, A. M. M., Bakar, N. F. A., Abidin, S. A. S. Z., Zain, Z. M. and Low, K. -F. (2023) A voltammetric immunosensor based on a nanoporous alumina millirod for detection of porcine serum albumin. *Food Chemistry*, **411**, 1–16.
 33. Kadam, V. V., Shanmugam, S. D., Ettiyappan, J. P. and Balakrishnan, R. M. (2021) Photocatalytic degradation of *p*-nitrophenol using biologically synthesized ZnO nanoparticles. *Environmental Science and Pollution Research*, **28**, 12119–12130.
 34. Seoudi, R. and Said, D. A. (2011) Studies on the effect of the capping materials on the spherical gold nanoparticles catalytic activity. *World Journal of Nano Science and Engineering*, **1**, 51–61.
 35. Swathy, T., Jinish Antony, M. and George, N. (2021) Active solvent hydrogen-enhanced *p*-nitrophenol reduction using heterogeneous silver nanocatalysts@surface-functionalized multiwalled carbon nanotubes. *Industrial & Engineering Chemistry Research*, **60**, 7050–7064.
 36. Wang, H., Dong, Z. and Na, C. (2013) Hierarchical carbon nanotube membrane-supported gold nanoparticles for rapid catalytic reduction of *p*-nitrophenol. *ACS Sustainable Chemistry & Engineering*, **1**, 746–752.
 37. Huang, X., Mutlu, H. and Théato, P. (2021) The toolbox of porous anodic aluminum oxide-based nanocomposites: from preparation to application. *Colloid and Polymer Science*, **299**, 325–341.
 38. Pongsanon, P., Kawamura, A., Kawasaki, H. and Miyata, T. (2024) Effect of gold nanoparticle size on regulated catalytic activity of temperature-responsive polymer-gold nanoparticle hybrid microgels. *Gels*, **10**, 357–373.
 39. Lin, C., Tao, K., Hua, D., Ma, Z. and Zhou, S. (2013) Size effect of gold nanoparticles in catalytic reduction of *p*-nitrophenol with NaBH₄. *Molecules*, **18**, 12609–12620.
 40. Naya, S. -I., Teranishi, M., Kimura, K. and Tada, H. (2011) A strong support-effect on the catalytic activity of gold nanoparticles for hydrogen peroxide decomposition. *Chemical Communications*, **47**, 3230–3232.
 41. Fu, M., Li, M., Zhao, Y., Bai, Y., Fang, X., Kang, X., Yang, M., Wei, Y. and Xu, X. (2021) A study on the high efficiency reduction of *p*-nitrophenol (4-NP) by a Fe(OH)₃/Fe₂O₃@ Au composite catalyst. *RSC Advances*, **11**, 26502–26508.
 42. Mejía, Y. R. and Reddy Bogireddy, N. K. (2022) Reduction of 4-nitrophenol using green-fabricated metal nanoparticles. *RSC Advances*, **12**, 18661–18675.